Korean J. Chem. Eng., 39(3), 695-705 (2022)
DOI: 10.1007/s11814-021-0893-2

pISSN: 0256-1115
eISSN: 1975-7220

Oxygen absorption and desorption properties of $YBaCo_4O_{7+\delta}$ monolithic oxygen carrier in the fixed-bed reactor

Limin Hou*,,†, Chaoyue Qiao**, Qingbo Yu***, and Wenfei Wu*,****

*Key Laboratory of Integrated Exploitation of Bayan Obo Multi-Metal Resources, Inner Mongolia University of Science and Technology, Inner Mongolia, China
**Key laboratory of Efficient and Clean Combustion, School of Energy and Environment, Inner Mongolia University of Science and Technology, Baotou, Inner Mongolia, P. R. China
***School of Metallurgy, Northeastern University, Shenyang, P. R. China
(*Received 8 April 2021 • Revised 2 July 2021 • Accepted 4 July 2021*)

Abstract−The technology of chemical looping air separation, with the characteristics of simple operation, low cost, and low energy consumption, separates oxygen from air with the oxygen carrier. In this work, reaction properties of monolithic oxygen carriers were investigated in a fixed-bed apparatus, with the consideration of the reactor temperature, oxygen concentration, and reaction gas flow. The XRD results showed that active phase, Al_2O_3, and cordierite cannot react with each other in calcination processing. The SEM results showed that the micromorphology of oxygen carrier was loaded on cordierite honeycomb uniformly with sphere or sphere-like particles. Oxygen carriers show a faster oxygen release rate and a slower oxygen intake rate. With increasing of absorption temperature, oxygen concentration of inlet gas, and desorption temperature, the reaction rate per unit mass increases. With increasing of gas flow rate, the reaction rate per unit mass decreases. The maximum value of the reaction rate per unit mass was obtained by $Y_{0.95}Ti_{0.05}BaCo_4O_{7+\delta}$ monolith sample. Samples substituted with Dy element showed fine performance of stability, as Dy substitution causes more serious local lattice distortions.

Keywords: Chemical Looping Air Separation, Monolithic Oxygen Carrier, Reactivity, Fixed-bed

INTRODUCTION

Chemical looping air separation (CLAS), a process of oxygen production proposed in 2010, has the superiority of low cost, extensive energy consumption and simple operation [1]. The CLAS process consumes 26% of the power of deep cooling process [2]. Oxygen carrier is one of the essences of CLAS system. The oxygen carrier takes oxygen from the air in an oxidation reactor and then releases the oxygen in a reduction reactor. The focus of oxygen carriers is metal oxide, sulfate, and perovskite [3-13]. Diego et al. investigated the combustion properties of CH_4 and H_2 with CuO oxygen carrier. The results showed that adding a supporter such as Al_2O_3, SiO_2, TiO_2, ZrO_2, and sepiolite can enhance the cyclic stability of oxygen carrier [3]. Wang et al. investigated the properties of coal reacted with CuO and Fe_2O_3 oxygen carriers. The results showed that combination of CuO and Fe_2O_3 is more conducive to combustion of coal than the CuO or Fe_2O_3. The CuO is reduced to Cu and Fe_2O_3 is reduced to Fe_3O_4 and FeO in the reduction reactor. The amount of CO_2 increases and the amount of H_2O decreases when the temperature is lower than 700 °C. The combustion trend is opposite when the temperature is higher than 700 °C [4]. Ge et al. investigated the biomass gasification properties with nickel-based oxygen carrier in a fixed bed reactor [5]. The results showed that the conversion efficiency increased in the temperature range of 650-680 °C, and the maximum value of syngas yield was reached at 750 °C. In addition, adding CaO can improve the syngas yield. Dou et al. investigated the hydrogen production properties of ethanol with Ni-based oxygen carrier in a fixed-bed reactor [6]. The results showed that the ethanol conversion increased with reaction time prolonged. The oxidation process of Ni-based oxygen carrier can be described by the shrinking core model. And the reduction rate is controlled by three stages. Mattisson et al. investigated the reaction properties of Mn_3O_4, CuO, and CoO oxygen carriers by the simulations method [7]. The results indicated that Mn_2O_3/Mn_3O_4 and CuO/Cu_2O oxygen carriers were the promising ones. CuO oxygen carrier reacting with gaseous and solid fuels showed excellent properties. Siriwardane et al. investigated the properties of coal reacted with CuO, Fe_2O_3, Co_3O_4, NiO, and Mn_2O_3 oxygen carriers with Al_2O_3 as binder, separately [8]. The results indicated that CuO oxygen carrier showed superb properties. The coal starts reduction reaction at 500 °C and combusts fully at 700 °C with CO_2 and H_2O generated. The Cu_2O can be oxidized fully to CuO at 700 °C. In the cyclic test, CuO oxygen carrier showed fine stability. CoO oxygen carrier showed bad reaction properties as generating $CoAl_2O_4$.

Tian and Guo studied the influence of temperature, pressure and oxygen ratio on the gaes process with $CaSO_4$ as oxygen carrier for CLC process system [9]. The optimal operating parameters, temperature of 750-950 °C, pressure of 1-15 bars, and oxygen ratio of 0.4-0.8, were obtained by the simulated results. The TG results

†To whom correspondence should be addressed.
E-mail: neuhlm@163.com
Copyright by The Korean Institute of Chemical Engineers.

showed that when the partial pressure of CO or H_2 was higher than 40 kPa, release of sulfurous gases could be avoided. Rydén et al. investigated reduction and oxidization reactivity of $LaFeO_{3-\delta}$, $La_{0.8}Sr_{0.2}FeO_{3-\delta}$, $La_{0.5}Sr_{0.5}FeO_{3-\delta}$, and $La_{0.5}Sr_{0.5}Fe_{0.5}Co_{0.5}O_{3-\delta}$ oxygen carriers added NiO, Fe_2O_3, and Mn_3O_4 as support [10]. The results indicated that the selectivity of CO and H_2 was high for $La_{0.8}Sr_{0.2}FeO_{3-\delta}$ and $La_{0.5}Sr_{0.5}FeO_{3-\delta}$ oxygen carriers. Nalbandian et al. studied the properties of syngas with $La_{1-x}Sr_xM_yFe_{1-y}O_3$ (M=Ni, Co, Cr, Cu) as oxygen carrier [11]. The results showed that adding NiO can enhance fuel reactivity and the selectivity for CO and H_2. $La_{0.7}Sr_{0.3}Cr_{0.05}Fe_{0.95}O_3$ sample mixed with 5% NiO showed the best performance in reaction stability and H_2 yields.

Oxide sulfate maybe release a harmful gas such as SO_2. Perovskite and metallic oxide oxygen carriers, reacting at high temperature, consume considerable amounts of energy. $YBaCo_4O_{7+\delta}$, reacting at low temperature, consumes less energy than that of metallic oxides [14,15]. Thus, $YBaCo_4O_{7+\delta}$ oxygen carrier for CLAS system not only can get oxygen with low energy consumption, but also can provide a fresh way for utilization of waste heat resources at temperature lower than 500 °C. Oxygen storage capacity of $YBaCo_4O_{7+\delta}$ is 1,225 μmol O_2/g, which is larger than that of oxygen storage material, CeO_2-ZrO_2 [16,17]. For the purpose of enhancing the oxygen storage capacity of oxygen carrier, researches on substitutions with Ca, Ti, Zr, Dy, Tb, Ho, Er, Lu, Yb, and Tm, in Y site and Zn, Mn, Ga, Al, Fe, and Cu in Co site of $YBaCo_4O_{7+\delta}$ were conducted [18-26]. The results showed that Ti, Zr, Dy, and Tb substitution had positive effects on enhancing the OSC. Very few studies focused on the preparation of monolithic $YBaCo_4O_{7+\delta}$ oxygen carrier and reaction properties of samples in a fixed reactor. Monolithic sample has shown sufficient activity and thermal dynamics stability under operating conditions of interest.

The $YBaCo_4O_{7+\delta}$ oxygen carriers are mostly reported in the form of particles mentioned above. In the work, the oxygen absorption and desorption properties of $YBaCo_4O_{7+\delta}$ monolithic oxygen carrier in fixed-bed reactor were deeply studied, with consideration of oxygen concentration, gas flow rate, absorption temperature, and desorption temperature. Moreover, the thermodynamic stability of monolithic samples was evaluated by characterizing XRD, SEM, and reaction properties of monoliths before and after cycle tests. The results in the work can provide the practical design operation parameters of $YBaCo_4O_{7+\delta}$ oxygen carrier for industrial application in the future.

EXPERIMENTAL SECTION

1. Preparation of Materials

Active phases, $YBaCo_4O_{7+\delta}$, $Y_{0.95}Ti_{0.05}BaCo_4O_{7+\delta}$, $Y_{0.5}Dy_{0.5}BaCo_4O_{7+\delta}$, $Y_{0.2}Ti_{0.05}Dy_{0.75}BaCo_4O_{7+\delta}$, were synthesized by the solid-state reaction. Starting material powders, thoroughly mixed with the appropriate stoichiometric amount, were calcined at 1,000 °C for 15 h. The calcined samples were ground and heated to 1,100 °C for 15 h, followed by the air-cooling [27]. Cordierite honeycombs, square aperture with 400 CPSI (channels per square inch) and wall thickness of 0.15 mm, were used as first carrier to support the second carrier (Al_2O_3 sol) and active phases. First, to purify the cordierite honeycombs, they were washed by deionized water and calcined at 900 °C for 2 h [28]. The active phase was coated on the cordierite honeycombs by dipping slurry with the slurry wash-coating method [29]. To get the effective slurry, we mixed the appropriate amount of active phase, Al_2O_3 sol and deionized water in ultrasonic vibration system [29], and adjusted the pH of slurry to 3.5 [30]. To get the desired amount of loading about 30 wt% of the cordierite honeycomb, several times of dipping slurry were needed [28]. And, the monolithic samples, dried at room temperature and dried overnight at 100 °C, were calcined at 550 °C for 3 h to stabilize γ-Al_2O_3.

2. Properties Evaluation and Characterization

The properties of monolithic samples are evaluated in the fixed-bed reactor (30 mm i.d. and 1,200 mm height). For oxygen absorption process, gas flow rates, oxygen concentration, and adsorption temperature are considered. For oxygen desorption process, desorption temperature is considered. The operating conditions are shown in Table 1. The monolithic samples are placed in the reactor supported by distributor plate [32]. The reaction gas is controlled by the mass flow controller. The concentration of outlet gas is analyzed by a gas analyzer. The schematic view of the experimental fix-bed system is showed elsewhere [27]. For oxygen intake process, to avoid oxygen absorption, the monolithic sample is heated to the desired temperature in N_2 atmosphere and then the gas is turned to absorption gas. After finishing the oxygen intake process, the sample is heated to the desired desorption temperature, then the gas is turned to N_2. The influence of air/N_2 in the system is eliminated by the data processing [32]. To investigate the stability and reactivity of the oxygen intake and release processes, cyclic experiments are performed at 350 °C and 430 °C upon switching the atmosphere from air to N_2 and *vice versa*. Data analysis is as follows [32,33]:

For the oxygen intake process, amount of oxygen intake (V_{oxi}) can be got by Eq. (1).

$$V_{oxi}=\int_0^{t_{oxi}}(Q_{out'}\times C_{out'}-Q_{out}\times C_{out})dt \quad (1)$$

where, Q_{out} and $Q_{out'}$ is the gas flow rate of the outlet with reaction

Table 1. The experiment operating conditions

Monolith sample	Absorption temperature/°C	Desorption temperature/°C	Gas flow/ (ml/min)	Oxygen concentration/%
$YBaCo_4O_{7+\delta}$	290	390	200	5.5
$Y_{0.95}Ti_{0.05}BaCo_4O_{7+\delta}$	310	450	400	10.5
$Y_{0.5}Dy_{0.5}BaCo_4O_{7+\delta}$	330	410	500	15.7
$Y_{0.2}Ti_{0.05}Dy_{0.75}BaCo_4O_{7+\delta}$	350	430	300	21

and without reaction, respectively, ml/min; C_{out} and $C_{out'}$ is the oxygen concentration of the outlet gas with reaction and without reaction, respectively, %; t_{oxi} is the oxygen intake time, min.

Based on conservation of N_2 flow for the inlet and outlet, Eq. (2) and Eq. (3) can be got.

$$Q_{in}\times(100-C_{in})=Q_{out}\times(100-C_{out}) \quad (2)$$

$$Q_{in}\times(100-C_{in})=Q_{out'}\times(100-C_{out'}) \quad (3)$$

Combined with the Eq. (1), Eq. (2) and Eq. (3), the following equation is got.

$$V_{oxi}=\int_0^{t_{oxi}}(100-C_{in})\times Q_{in}\times\left(\frac{C_{out'}-C_{out}}{(1-C_{out})(1-C_{out'})}\right)dt \quad (4)$$

Reaction rate of oxygen intaking (v_{oxi}) can be got by Eq. (5).

$$v_{oxi}=\frac{V_{oxi}}{t_{oxi}} \quad (5)$$

For the oxygen desorption process, amount of oxygen releasing (V_{red}) can be got by Eq. (6).

$$V_{red}=\int_0^{t_{red}}100\times Q_{in}\times\left(\frac{C_{out'}-C_{out}}{(1-C_{out})(1-C_{out'})}\right)dt \quad (6)$$

where, t_{red} is the oxygen releasing time, min.

Reaction rate of oxygen releasing can be got by Eq. (7).

$$v_{red}=\frac{V_{red}}{t_{red}} \quad (7)$$

X-ray diffraction of the samples is performed in a PANalytical X'Pert Pro PW 3040/60 with 2θ of 10°-70°. SUPERSCAN SSX-550 spectrometer system is used to observe the microstructure of the samples.

RESULTS AND DISCUSSION

1. Results and Analysis of XRD and SEM Characterization

Fig. 1(a) and 1(b) show the phase composition of γ-Al_2O_3, γ-Al_2O_3 and cordierite. Fig. 1(c) shows the phase composition of $YBaCo_4O_{7+\delta}$, $Y_{0.95}Ti_{0.05}BaCo_4O_{7+\delta}$, $Y_{0.5}Dy_{0.5}BaCo_4O_{7+\delta}$ and $Y_{0.2}Ti_{0.05}Dy_{0.75}BaCo_4O_{7+\delta}$ monolith sample. Fig. 1(a) shows that the Al_2O_3

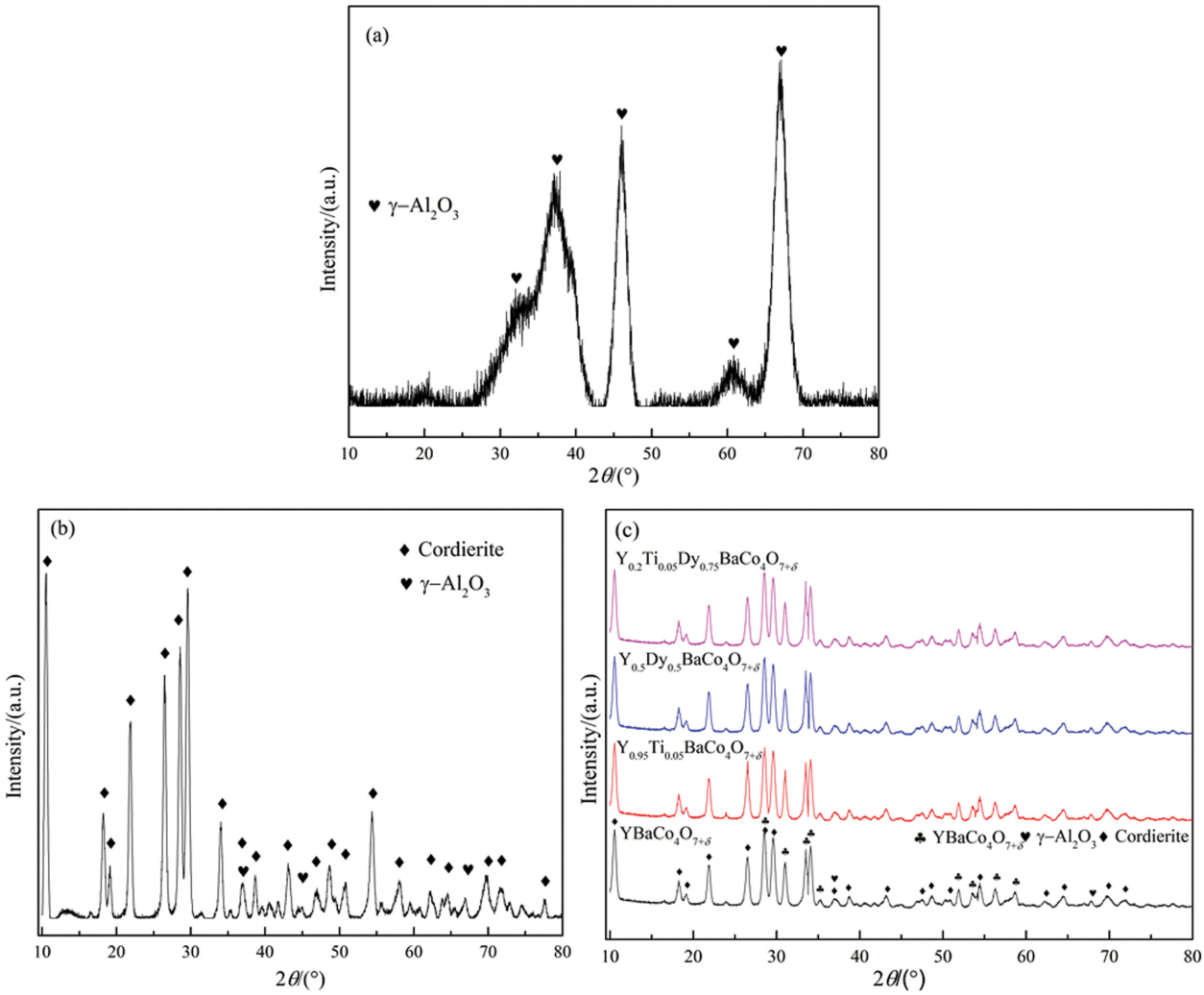


Fig. 1. Phase composition of (a) γ-Al_2O_3, (a) γ-Al_2O_3 and cordierite, and (c) $YBaCo_4O_{7+\delta}$, $Y_{0.95}Ti_{0.05}BaCo_4O_{7+\delta}$, $Y_{0.5}Dy_{0.5}BaCo_4O_{7+\delta}$, $Y_{0.2}Ti_{0.05}Dy_{0.75}BaCo_4O_{7+\delta}$ monolith samples.

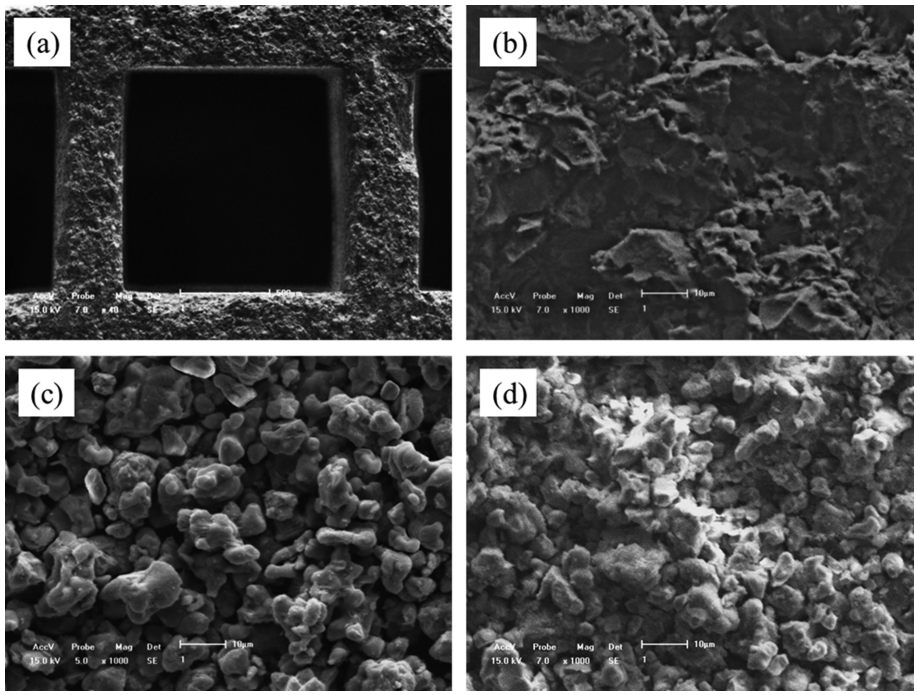


Fig. 2. SEM of (a) and (b) cordierite honeycomb, (c) $YBaCo_4O_{7+\delta}$ monolith sample, and (d) $Y_{0.5}Dy_{0.5}BaCo_4O_{7+\delta}$ monolith sample.

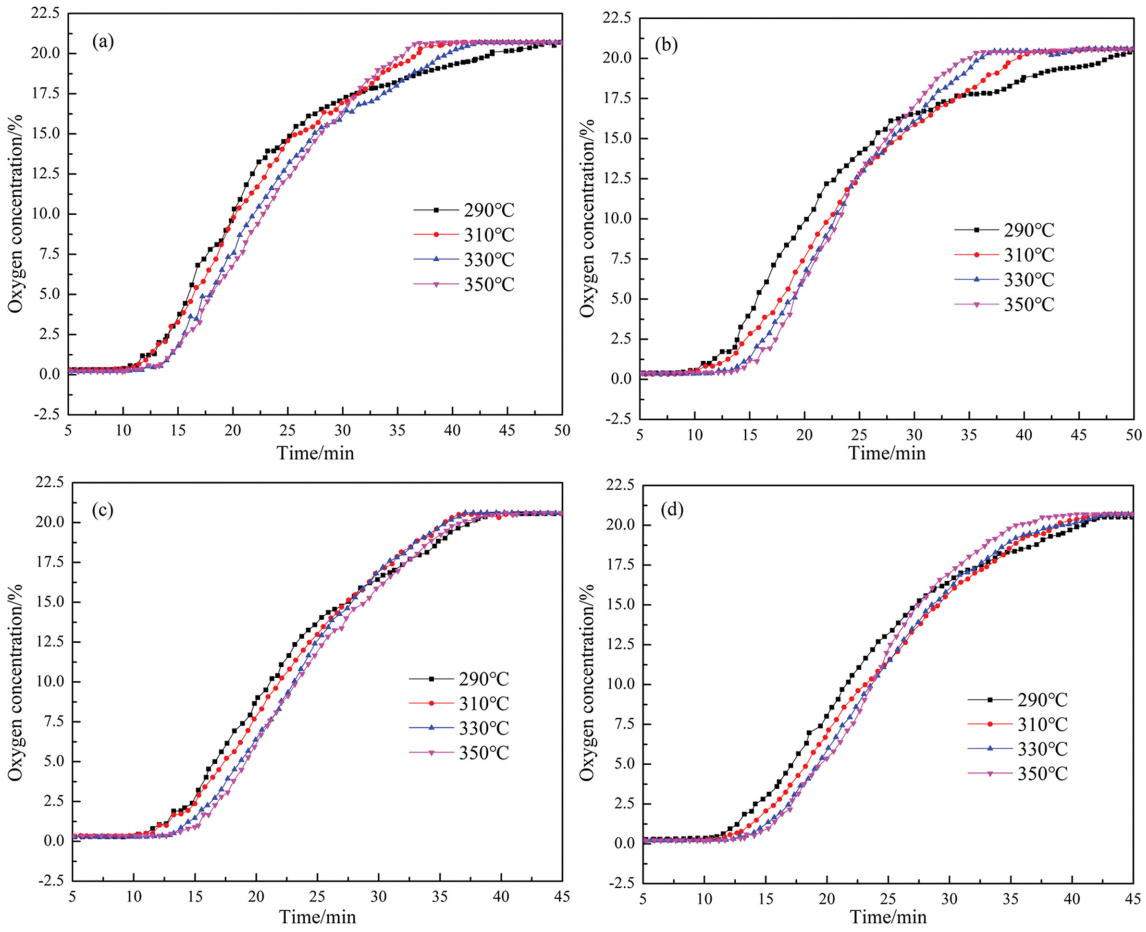


Fig. 3. Outlet oxygen concentration of (a) $YBaCo_4O_{7+\delta}$, (b) $Y_{0.95}Ti_{0.05}BaCo_4O_{7+\delta}$, (c) $Y_{0.5}Dy_{0.5}BaCo_4O_{7+\delta}$, and (d) $Y_{0.2}Ti_{0.05}Dy_{0.75}BaCo_4O_{7+\delta}$ monolith samples at different temperatures.

Table 2. Amount of oxygen intake per unit mass at different conditions

Variable		Amount of oxygen intake per unit mass/ml/(min·g)			
		$YBaCo_4O_{7+\delta}$	$Y_{0.95}Ti_{0.05}BaCo_4O_{7+\delta}$	$Y_{0.5}Dy_{0.5}BaCo_4O_{7+\delta}$	$Y_{0.2}Ti_{0.05}Dy_{0.75}BaCo_4O_{7+\delta}$
Absorption temperature/°C	290	13.057	13.753	13.230	13.734
	310	15.477	16.380	16.023	15.892
	330	15.708	16.591	16.205	16.041
	350	14.861	15.515	15.477	15.192
Gas flow/ (ml/min)	200	14.861	15.515	15.477	15.192
	300	14.224	14.551	14.468	14.357
	400	10.838	11.720	11.199	10.929
	500	8.255	9.365	8.609	8.533
Oxygen concentration/%	5.25	3.575	3.855	3.757	3.747
	10.5	7.020	8.594	8.446	8.371
	15.7	10.644	10.921	10.878	10.731
	21.0	14.861	15.515	15.477	15.192

gel has formed the γ-Al_2O_3 after being calcined at 550 °C. γ-Al_2O_3 and cordierite are identified in Fig. 1(b). γ-Al_2O_3, cordierite, $YBaCo_4O_{7+\delta}$, $Y_{0.95}Ti_{0.05}BaCo_4O_{7+\delta}$, $Y_{0.5}Dy_{0.5}BaCo_4O_{7+\delta}$, and $Y_{0.2}Ti_{0.05}Dy_{0.75}BaCo_4O_{7+\delta}$ are identified in Fig. 1(c), indicating that active phase, Al_2O_3, and cordierite cannot react in the calcination process.

Fig. 2(a) and 2(b) display the micromorphology of cordierite honeycomb. Fig. 2(c) and 2(d) display the micromorphology of $YBaCo_4O_{7+\delta}$ and $Y_{0.5}Dy_{0.5}BaCo_4O_{7+\delta}$ monolith sample at 1,000× magnification, respectively. Fig. 2(a) shows that the micromorphology of cordierite honeycomb is uneven polyhedron. Fig. 2(b) shows that the micromorphology of oxygen carrier loaded uniformly is sphere or sphere-like particles. Active phase, $YBaCo_4O_{7+\delta}$, $Y_{0.95}Ti_{0.05}BaCo_4O_{7+\delta}$, $Y_{0.5}Dy_{0.5}BaCo_4O_{7+\delta}$, $Y_{0.2}Ti_{0.05}Dy_{0.75}BaCo_4O_{7+\delta}$ are synthetized at 1,150 °C with 30 h. The crystal structure is very stable in phase and micromorphology and difficult to react with other substances. The $YBaCo_4O_{7+\delta}$ oxygen carriers are reported in the form of particles [18-26]. Particles of oxygen carriers are made the monolithic samples without damaging the phase and morphology.

2. Results and Analysis of Reactivity Properties

Fig. 3 shows the outlet oxygen concentration under different absorption temperature of all monolith samples. The outlet oxygen concentration increases with prolonging of oxygen intake. The outlet oxygen concentration is maintained near the inlet oxygen concentration at the end of the oxygen intake. For the same time, the outlet oxygen concentration obtained is different at different absorption temperatures. Based on the data of outlet oxygen concentration, the amount of oxygen intake per unit mass at different temperatures can be got, shown in Table 2.

With increasing of temperature, the amount of oxygen intake per unit mass increases first and then decreases. All the oxygen carriers start to absorb oxygen and stop to absorb oxygen at the time of 10-15 min and 35-50 min under different temperatures, respectively. There is a bigger difference for completion time of oxygen absorption and starting time for oxygen carrier. For $Y_{0.5}Dy_{0.5}BaCo_4O_{7+\delta}$ monolith sample, the amount of oxygen intake per unit mass is 13.230 ml/g, 16.023 ml/g, 16.205 ml/g, and 15.477 ml/g obtained at temperature of 290 °C, 310 °C, 330 °C, and 350 °C, respectively. 330 °C is the most suitable for oxygen carrier to absorb oxygen. Oxygen storage capacity per unit mass of $YBaCo_4O_{7+\delta}$ and $Y_{0.5}Dy_{0.5}BaCo_4O_{7+\delta}$ is not lower than that of reported $YBaCo_4O_{7+\delta}$ in the form of particle [18-21], indicating that the synthesis and operating parameters are appropriate. At the same temperature, the amount of oxygen intake per unit mass varies in the order: $Y_{0.95}Ti_{0.05}BaCo_4O_{7+\delta}$>$Y_{0.5}Dy_{0.5}BaCo_4O_{7+\delta}$>$Y_{0.2}Ti_{0.05}Dy_{0.75}BaCo_4O_{7+\delta}$>$YBaCo_4O_{7+\delta}$ monolith samples. The oxygen storage capacity varies in the order: $Y_{0.5}Dy_{0.5}BaCo_4O_{7+\delta}$>$Y_{0.2}Ti_{0.05}Dy_{0.75}BaCo_4O_{7+\delta}$>$Y_{0.95}Ti_{0.05}BaCo_4O_{7+\delta}$>$YBaCo_4O_{7+\delta}$ samples [26]. The order of amount of oxygen intaking per unit mass and amount of oxygen storage capacity is different as the relative micro molecular weight of doped elements is different.

With increasing of temperature, the reaction rate of oxygen intaking per unit mass increases, shown in Fig. 4. For $Y_{0.5}Dy_{0.5}BaCo_4O_{7+\delta}$ monolith sample, the reaction rate of oxygen intake per unit mass is 0.272 ml/(min·g), 0.364 ml/(min·g), 0.396 ml/(min·g), and 0.408 ml/(min·g) obtained at temperature of 290 °C, 310 °C, 330 °C, and 350 °C, respectively. At the same temperature,

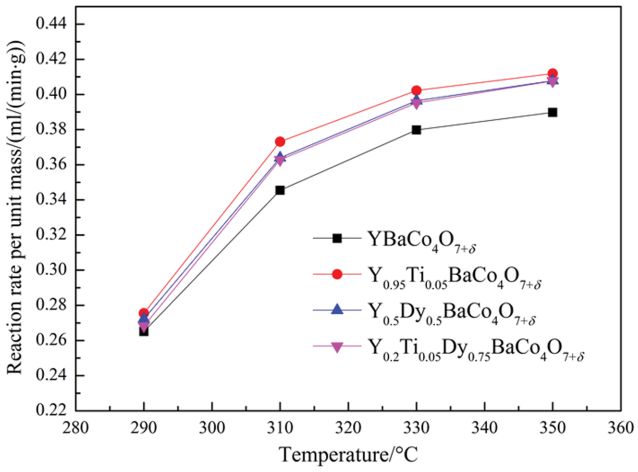


Fig. 4. Reaction rate per unit mass of oxygen carrier at different temperatures.

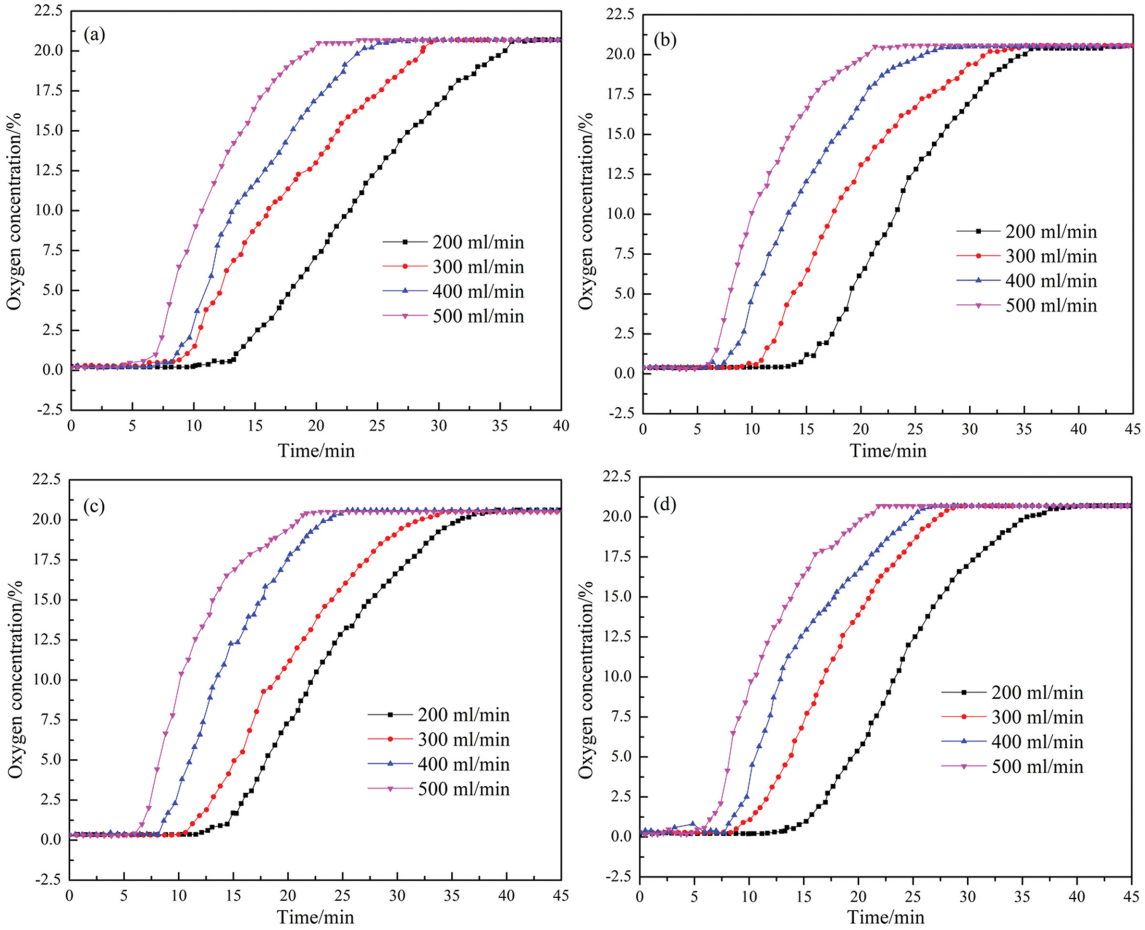


Fig. 5. Outlet oxygen concentration of (a) $YBaCo_4O_{7+\delta}$ (b) $Y_{0.95}Ti_{0.05}BaCo_4O_{7+\delta}$ (c) $Y_{0.5}Dy_{0.5}BaCo_4O_{7+\delta}$ and (d) $Y_{0.2}Ti_{0.05}Dy_{0.75}BaCo_4O_{7+\delta}$ monolith samples at different gas flow rates.

the reaction rate of oxygen intake per unit mass varies in the same order as the amount of oxygen intake per unit mass.

Fig. 5 shows the outlet oxygen concentration under gas flows during oxygen absorption process of all monolith samples. The outlet oxygen concentration increases to the value of inlet oxygen concentration with prolonging of oxygen intake. The larger the gas flow, the earlier the oxygen carrier starts to absorb oxygen and the shorter the oxygen carrier completes to absorb oxygen. The outlet oxygen concentration increases with increasing the gas flow rate. The amount of oxygen intake per unit mass at different gas flow rates can be determined, shown in Table 2. For $Y_{0.5}Dy_{0.5}BaCo_4O_{7+\delta}$ monolith sample, the amount of oxygen intake per unit mass is 15.477 ml/g, 14.468 ml/g, 11.199 ml/g, and 8.609 ml/g obtained at flow rate of 200 ml/min, 300 ml/min, 400 ml/min, and 500 ml/min, respectively. The amount of oxygen intake per unit mass decreases as gas flow rate increases. The reason for this is that there is less oxygen reacting with oxygen carrier in unit time when gas flow rate increases. The amount of oxygen intake per unit mass of monolith sample obtained at same gas flow rate varies in same order as absorption temperature.

With increasing of gas flow rate, the reaction rate of oxygen intake per unit mass decreases, shown in Fig. 6. For $Y_{0.5}Dy_{0.5}BaCo_4O_{7+\delta}$ monolith sample, the reaction rate of oxygen intake per unit mass

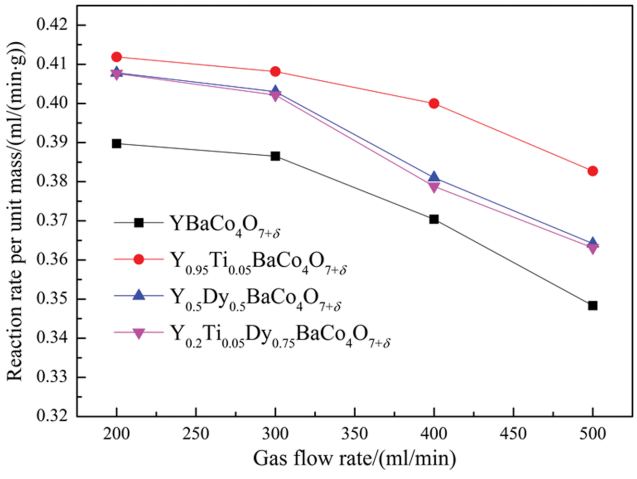


Fig. 6. Reaction rate per unit mass of oxygen carrier at different gas flow rates.

is 0.408 ml/(min·g), 0.403 ml/(min·g), 0.381 ml/(min·g), and 0.364 ml/(min·g) obtained at gas flow rate of 200 ml/min, 300 ml/min, 400 ml/min, and 500 ml/min, respectively. At the same gas flow rate, the reaction rate of oxygen intake per unit mass of monolith

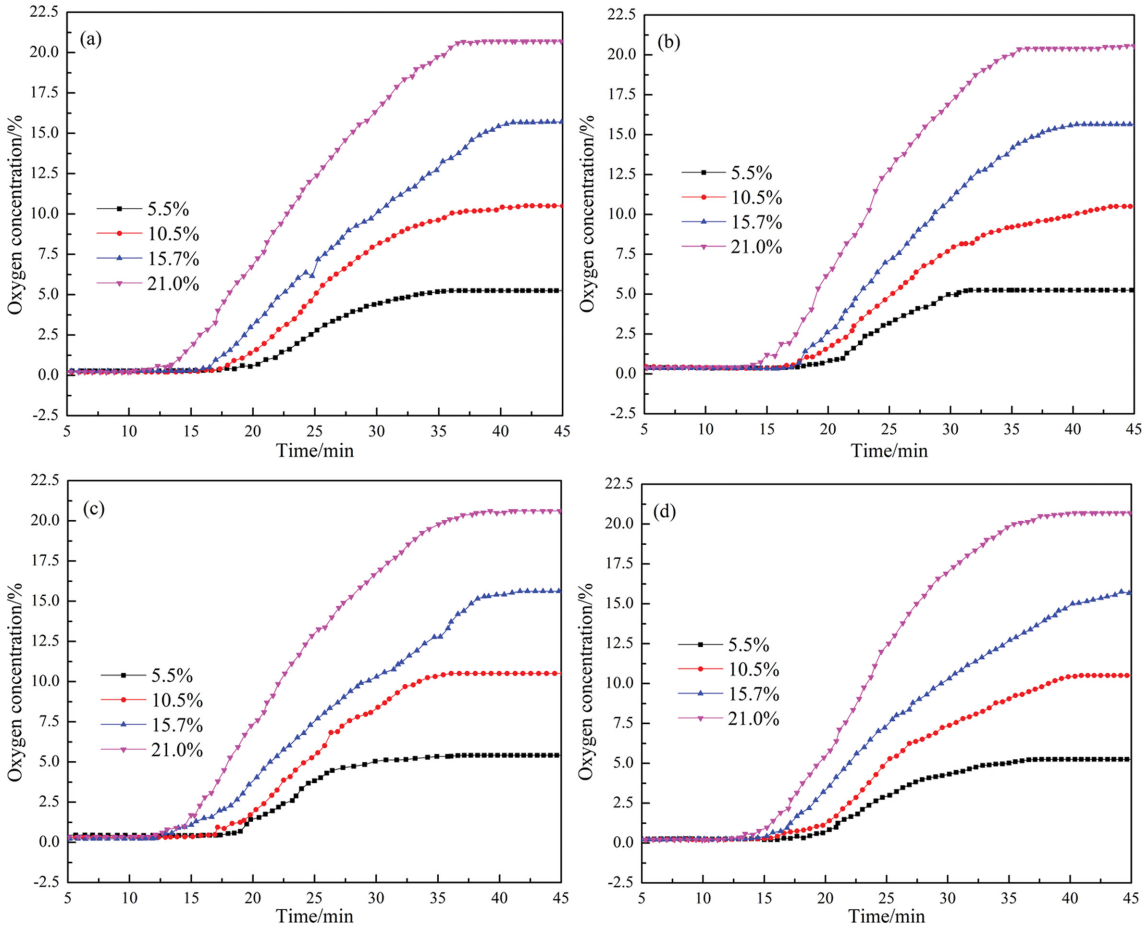


Fig. 7. Outlet oxygen concentration of (a) $YBaCo_4O_{7+\delta}$, (b) $Y_{0.95}Ti_{0.05}BaCo_4O_{7+\delta}$, (c) $Y_{0.5}Dy_{0.5}BaCo_4O_{7+\delta}$ and (d) $Y_{0.2}Ti_{0.05}Dy_{0.75}BaCo_4O_{7+\delta}$ monolith samples at different oxygen concentrations of inlet gas.

samples varies in same order as absorption temperature.

Fig. 7 shows the outlet oxygen concentration under oxygen concentration of inlet gas during oxygen absorption process of all monolith samples. The outlet oxygen concentration increases to the value of inlet oxygen concentration with prolonging oxygen intake. The outlet oxygen concentration increases with increasing the oxygen concentration of inlet gas. The amount of oxygen intake per unit mass at different oxygen concentrations of inlet gas can be got, shown in Table 2. For $Y_{0.5}Dy_{0.5}BaCo_4O_{7+\delta}$ monolith sample, the amount of oxygen intake per unit mass is 3.855 ml/g, 8.594 ml/g, 10.921 ml/g, and 15.515 ml/g obtained at oxygen concentration of 5.5%, 10.5%, 15.7%, and 21%, respectively. The amount of oxygen intake per unit mass increases with oxygen concentration increases for certain monolith sample. The reason for this is that there is more oxygen reacting with oxygen carrier in unit time when oxygen concentration increases. More oxygen is favored for the absorption process in certain time for oxygen carrier. The amount of oxygen intake per unit mass of monolith samples obtained at same oxygen concentration varies in same order as absorption temperature.

With increasing of oxygen concentration of inlet gas, the reaction rate of oxygen intake per unit mass increases, shown in Fig. 8. For, $Y_{0.5}Dy_{0.5}BaCo_4O_{7+\delta}$ monolith sample, the reaction rate of oxygen intake per unit mass is 0.118 ml/(min·g), 0.199 ml/(min·g), 0.274 ml/(min·g), and 0.412 ml/(min·g) obtained at oxygen concentration of 5.5%, 10.5%, 15.7%, and 21%, respectively. At the same oxygen concentration, the reaction rate of oxygen intake per unit

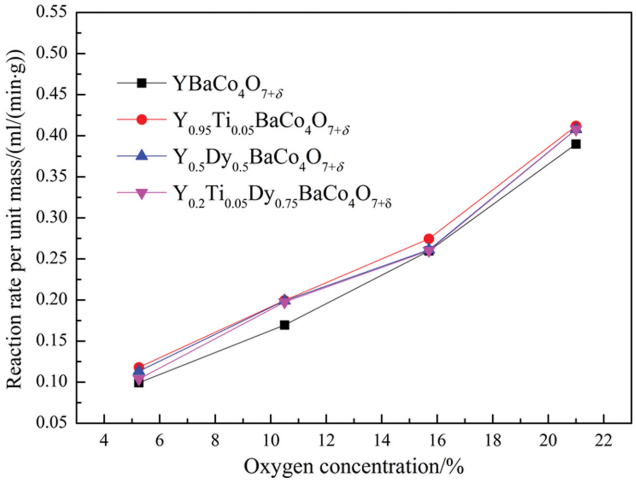


Fig. 8. Reaction rate per unit mass of oxygen carrier at different oxygen concentrations of inlet gas.

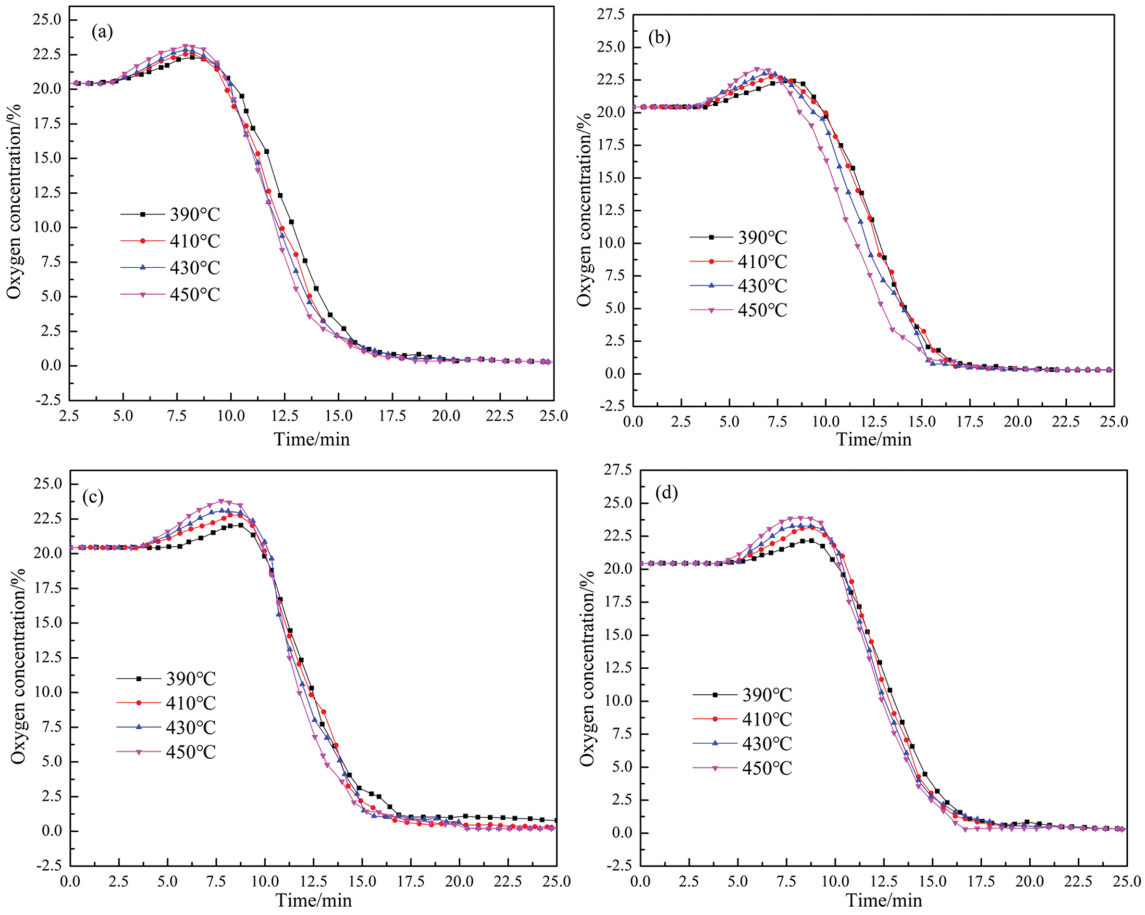


Fig. 9. Outlet oxygen concentration of (a) $YBaCo_4O_{7+\delta}$, (b) $Y_{0.95}Ti_{0.05}BaCo_4O_{7+\delta}$, (c) $Y_{0.5}Dy_{0.5}BaCo_4O_{7+\delta}$ and (d) $Y_{0.2}Ti_{0.05}Dy_{0.75}BaCo_4O_{7+\delta}$ monolith samples at different desorption temperatures.

mass of monolith samples varies in same order as absorption temperatures (Except the value obtained at 15.7% for $Y_{0.2}Ti_{0.05}Dy_{0.75}BaCo_4O_{7+\delta}$ monolith sample).

Fig. 9 shows the outlet oxygen concentration under desorption temperature of all monolith samples. The outlet oxygen concentration increases first and then decreases to the value of inlet oxygen concentration with prolonging oxygen release. The oxygen of intake can fully release at different temperatures. All the oxygen carriers start to desorb oxygen and stop to desorb oxygen at the time of 3-5 min and 17 min under all the temperatures, respectively. Oxygen carriers show a faster oxygen release rate and a slower oxygen intake rate.

With increasing of oxygen concentration of inlet gas, the reaction rate of oxygen release per unit mass increases, shown in Fig. 10. Increasing desorption temperature is in favor of oxygen releasing. For, $Y_{0.5}Dy_{0.5}BaCo_4O_{7+\delta}$ monolith sample, the reaction rate of oxygen release per unit mass is 0.696 ml/(min·g), 0.828 ml/(min·g), 0.916 ml/(min·g), and 0.938 ml/(min·g) obtained at temperature of 390 °C, 410 °C, 430 °C, and 450 °C, respectively. At the same temperature, the reaction rate of oxygen release per unit mass of monolith samples varies in same order as absorption temperatures (Except the value obtained at 450 °C for $Y_{0.2}Ti_{0.05}Dy_{0.75}BaCo_4O_{7+\delta}$ monolith sample).

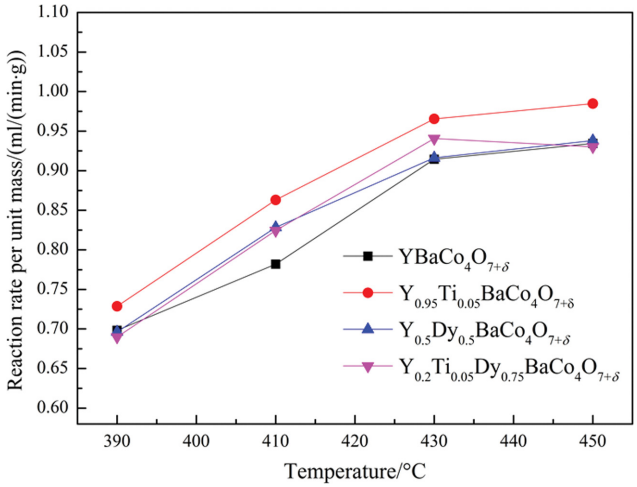


Fig. 10. Reaction rate per unit mass of oxygen carrier at different desorption temperatures.

3. Results and Analysis of Cyclic Stability

Fig. 11 shows the outlet oxygen concentration under absorption temperature of 350 °C and desorption temperature of 430 °C of monolith samples. The outlet oxygen concentration increases

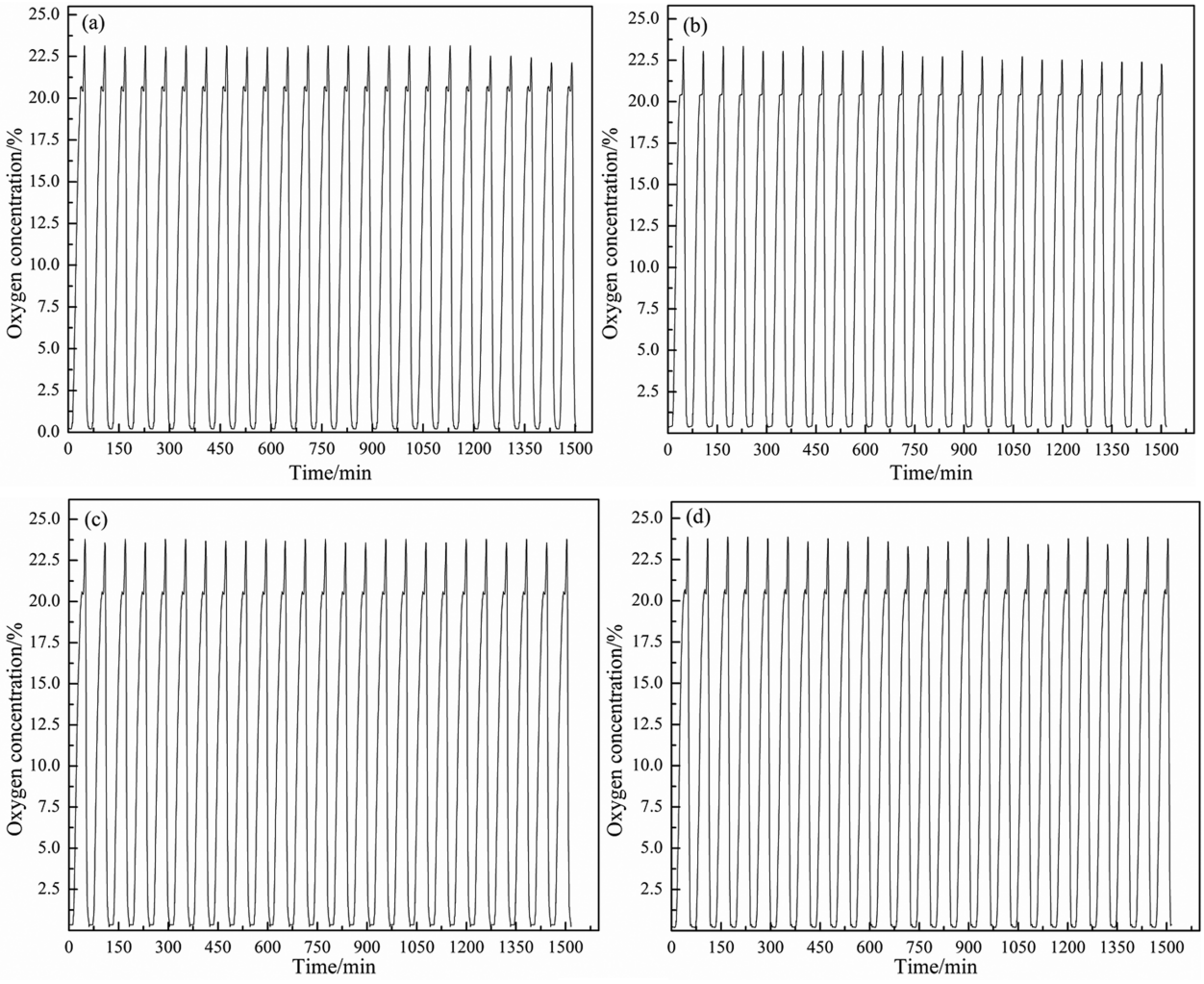


Fig. 11. Outlet oxygen concentration of (a) $YBaCo_4O_{7+\delta}$, (b) $Y_{0.95}Ti_{0.05}BaCo_4O_{7+\delta}$, (c) $Y_{0.5}Dy_{0.5}BaCo_4O_{7+\delta}$, and (d) $Y_{0.2}Ti_{0.05}Dy_{0.75}BaCo_4O_{7+\delta}$ monolith samples in cyclic tests.

first and then decreases to the value of inlet oxygen concentration with reaction prolonging. The maximum value of outlet oxygen concentration decreases after 20 cyclic tests for $YBaCo_4O_{7+\delta}$ and $Y_{0.95}Ti_{0.05}BaCo_4O_{7+\delta}$ sample, indicating that performance degradation occurs. The maximum value of outlet oxygen concentration maintains stability in 25 cyclic tests for $Y_{0.5}Dy_{0.5}BaCo_4O_{7+\delta}$ and $Y_{0.2}Ti_{0.05}Dy_{0.75}BaCo_4O_{7+\delta}$ sample, indicating that $Y_{0.5}Dy_{0.5}BaCo_4O_{7+\delta}$ and $Y_{0.2}Ti_{0.05}Dy_{0.75}BaCo_4O_{7+\delta}$ sample shows good cyclic stability. The amount of oxygen intake per unit mass for $YBaCo_4O_{7+\delta}$ sample in 20 cyclic tests is 14.5-14.9 ml/g. The smallest amount of oxygen intake per unit mass for $YBaCo_4O_{7+\delta}$ sample after 20 cyclic tests is 11.9 ml/g. The amount of oxygen intake per unit mass for $Y_{0.95}Ti_{0.05}BaCo_4O_{7+\delta}$ sample in 20 cyclic tests is 14.1-15.5 ml/g. The smallest amount of oxygen intake per unit mass for $YBaCo_4O_{7+\delta}$ sample after 18 cyclic tests is 12.3 ml/g. The amount of oxygen intake per unit mass for $Y_{0.5}Dy_{0.5}BaCo_4O_{7+\delta}$ and $Y_{0.2}Ti_{0.05}Dy_{0.75}BaCo_4O_{7+\delta}$ samples in 25 cyclic tests is 15.2-15.5 ml/g and 14.5-15.2 ml/g, respectively.

To investigate the reason for performance degradation of $YBaCo_4O_{7+\delta}$ and $Y_{0.95}Ti_{0.05}BaCo_4O_{7+\delta}$ samples, the XRD and SEM for samples before and after cyclic tests were conducted. Fig. 12 shows the phase composition of the samples before and after cyclic tests. The results show that there is no phase transition before and after cyclic tests. Fig. 13 shows the micromorphology of $YBaCo_4O_{7+\delta}$ and $Y_{0.5}Dy_{0.5}BaCo_4O_{7+\delta}$ before and after cyclic tests. From Fig. 13(a) and 13(b), $YBaCo_4O_{7+\delta}$ experiences extensive cracking and agglomerate, including fracture of some grains. Agglomeration is the macroscopic manifestation of sintering of grains. The cracking and agglomeration of sample restricts the gas flow, which is the reason accounted for performance degradation of $YBaCo_4O_{7+\delta}$ and $Y_{0.95}Ti_{0.05}BaCo_4O_{7+\delta}$ samples. There is no cracking and agglomeration for $Y_{0.5}Dy_{0.5}BaCo_4O_{7+\delta}$ sample, shown in the Fig. 13(c) and 13(d). The unit cell volume of $YBaCo_4O_{7+\delta}$, $Y_{0.95}Ti_{0.05}BaCo_4O_{7+\delta}$, $Y_{0.5}Dy_{0.5}BaCo_4O_{7+\delta}$, and $Y_{0.2}Ti_{0.05}Dy_{0.75}BaCo_4O_{7+\delta}$ is 349.4661 $Å^3$, 349.3005 $Å^3$, 351.2900 $Å^3$ and 350.6864 $Å^3$, respectively. The local lattice distortions, caused by the Dy substitution and Ti and Dy co-substitution, are larger than that of Ti substitution, which can inhibit the movement of grain of oxygen carrier. This probably accounted for the good cyclic stability of $Y_{0.5}Dy_{0.5}BaCo_4O_{7+\delta}$ and $Y_{0.2}Ti_{0.05}Dy_{0.75}BaCo_4O_{7+\delta}$ samples [35].

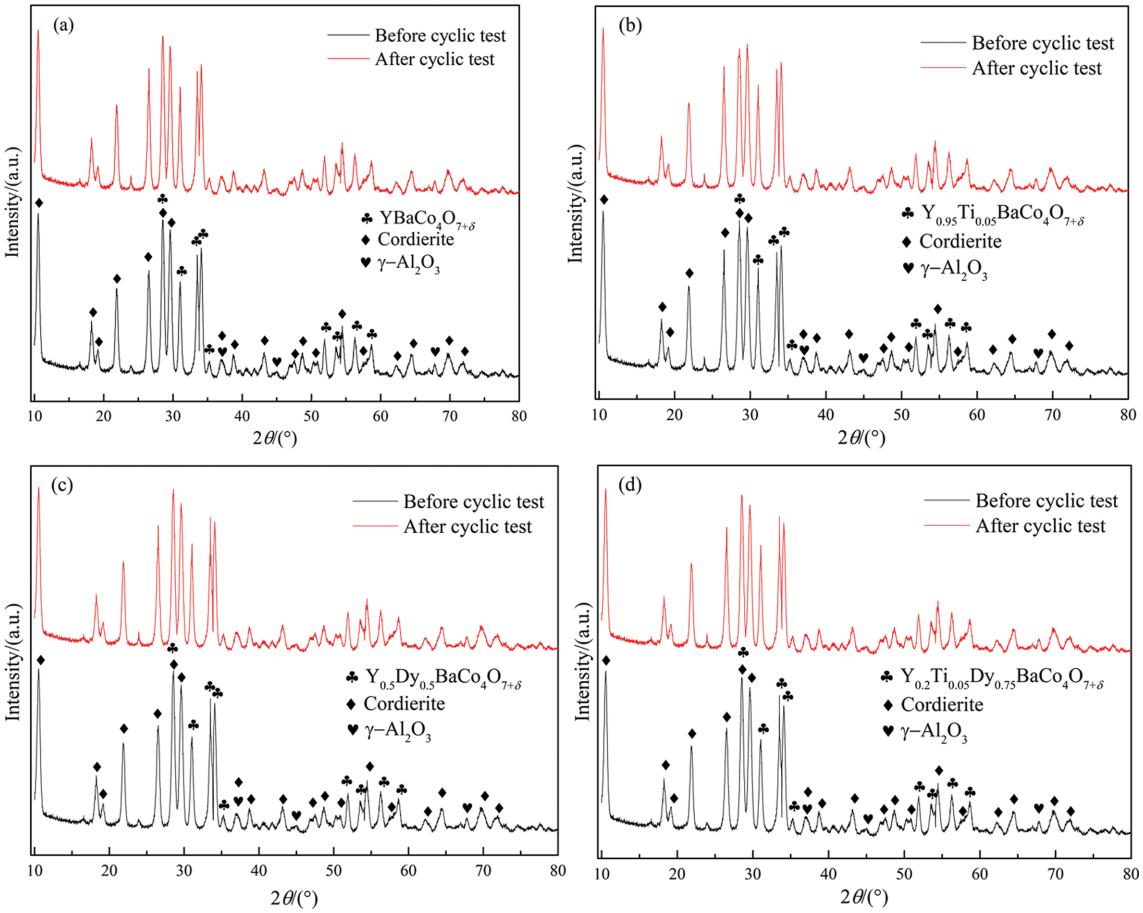


Fig. 12. The phase composition of (a) $YBaCo_4O_{7+\delta}$, (b) $Y_{0.95}Ti_{0.05}BaCo_4O_{7+\delta}$, (c) $Y_{0.5}Dy_{0.5}BaCo_4O_{7+\delta}$, and (d) $Y_{0.2}Ti_{0.05}Dy_{0.75}BaCo_4O_{7+\delta}$ monolith samples before and after cyclic tests.

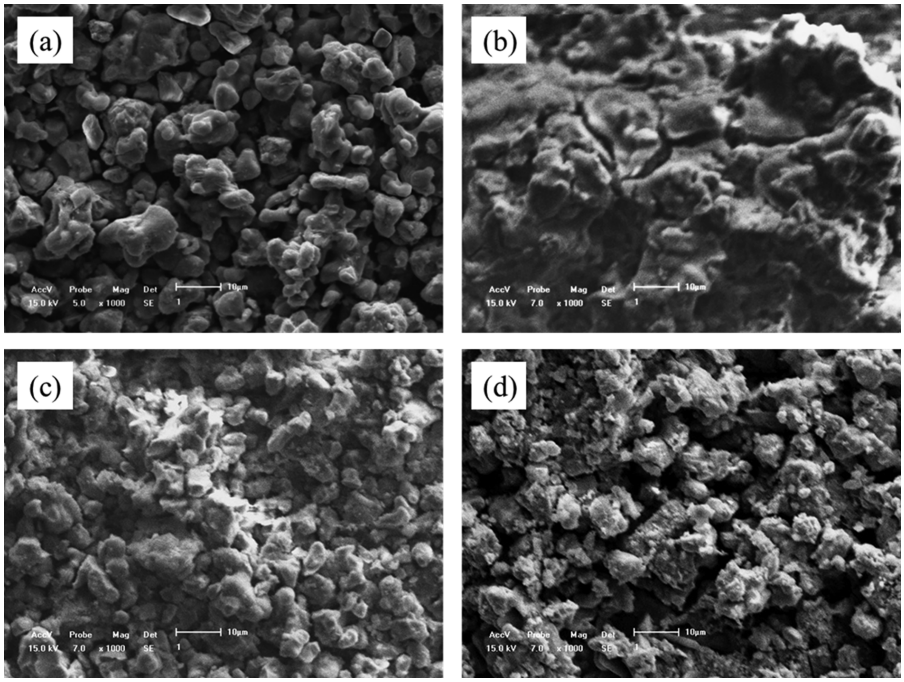


Fig. 13. The SEM of (a) $YBaCo_4O_{7+\delta}$ before cyclic tests, (b) $YBaCo_4O_{7+\delta}$ after cyclic tests, (c) $Y_{0.5}Dy_{0.5}BaCo_4O_{7+\delta}$ before cyclic tests, (d) $Y_{0.5}Dy_{0.5}BaCo_4O_{7+\delta}$ after cyclic tests.

CONCLUSIONS

In this work, the reaction properties of $YBaCo_4O_{7+\delta}$, $Y_{0.95}Ti_{0.05}BaCo_4O_{7+\delta}$, $Y_{0.5}Dy_{0.5}BaCo_4O_{7+\delta}$, and $Y_{0.2}Ti_{0.05}Dy_{0.75}BaCo_4O_{7+\delta}$ monolithic oxygen carriers were studied. Particles of oxygen carrier can be made monolithic samples without damaging the phase and morphology. Oxygen carriers show a faster oxygen release rate and a slower oxygen intake rate. With increasing of absorption temperature, the amount of oxygen intake per unit mass increases first and then decreases and the reaction rate of oxygen intake per unit mass increases. With increasing of gas flow rate, the amount of oxygen intake per unit mass and the reaction rate of oxygen intake per unit mass decreases. With increasing of oxygen concentration of inlet gas, the amount of oxygen intake per unit mass and the reaction rate of oxygen intake per unit mass increases. The maximum values of the amount of oxygen intake per unit mass and the reaction rate of oxygen intake per unit mass are obtained by $Y_{0.95}Ti_{0.05}BaCo_4O_{7+\delta}$ monolith sample. The absorbed oxygen can be released fully at different desorption temperatures. With increasing of desorption temperature, the reaction rate of oxygen release per unit mass increases. Cyclic stability of $Y_{0.5}Dy_{0.5}BaCo_4O_{7+\delta}$ and $Y_{0.2}Ti_{0.05}Dy_{0.75}BaCo_4O_{7+\delta}$ samples is better than that of $YBaCo_4O_{7+\delta}$ and $Y_{0.95}Ti_{0.05}BaCo_4O_{7+\delta}$ samples. The local lattice distortions, caused by substitution, can inhibit the movement of grain of oxygen carrier.

ACKNOWLEDGEMENTS

This study was financially supported by Natural Science Foundation of Inner Mongolia (Grant No. 2020BS05030, 2019ZD13), National Key Research and Development Project (Grant No. 2020 YFC1909102), and National Natural Science Foundation of China (Grant No. 51866013, 51576035). Thanks for Start-up Funds for Talent Introduction and Scientific Research of Institutions in Inner Mongolia Autonomous Region.

NOTES

The authors declare no competing financial interest.

REFERENCES

1. B. Moghtaderi, *Energy Fuels*, **24**(1), 190 (2010).
2. H. Song, K. Shah, E. Doroodchi and B. Moghtaderi, *Energy Fuels*, **28**(1), 163 (2014).
3. L. F. DE Diego, F. Gacía-labiano, J. Adáneza, P. Gayán, A. Abad, B. M. Corbella and J. M. Palacios. *Fuel*, **83**(13), 17490 (2004).
4. N. Son, J. Y. Do, N. Park, U. S. Kim, J. Baek, D. Lee, H. Ryu and M. Kang, *Korean J. Chem. Eng.*, **36**(12), 1971 (2019).
5. H. J. Ge, L. H. Shen, F. Feng and S. X. Jiang, *Appl. Therm. Eng.*, **85**, 52 (2015).
6. Y. Gao, J. Xiao, J. D. Ye and Y. T. Shen, *Korean J. Chem. Eng.*, **37**(1), 54 (2020).
7. T. Mattisson, A. Lyngfelt and H. Leion, *Int. J. Greenhouse Gas Control.*, **3**(1), 11 (2009).
8. R. Siriwardane, H. J. Tian, G. Richards, T. Simonyi and P. James, *Energy Fuels*, **23**(8), 3885 (2009).
9. H. Tian and Q. Guo, *Chem. Eng. Res. Des.*, **89**(9), 1524 (2011).
10. M. Rydén, A. Lyngfelt, T. Mattisson, D. Chen, A. Holmen and E. Bjørgum, *Int. J. Greenhouse Gas Control*, **2**(1), 21 (2008).
11. L. Nalbandian, A. Evdou and V. Zaspalis, *Int. J. Hydrogen Energ.*, **36**(11), 6657 (2011).
12. B. Y. Li, W. Zhang, Y. Q. Qian and Z. Y. Wang, *Korean J. Chem. Eng.*, **37**(4), 688 (2020).
13. Y. R. Gwak, J. H. Yun, S. I. Keel and S. H. Lee, *Korean J. Chem. Eng.*, **37**(11), 1878 (2020).
14. T. Mattisson, A. Lyngfelt and H. Leion, *Int. J. Greenhouse Gas Control*, **3**(1), 11 (2009).
15. M. Arjmand, A. Azad, H. Leion, A. Lyngfelt and T. Mattisson, *Energy Fuels*, **25**(11), 5493 (2011).
16. Y. Nagai, T. Yamamoto, T. Tanaka, S. Yoshida, T. Nonaka, T. Okamoto, A. Suda and M. Sugiura, *Catal. Today*, **74**(3-4), 225 (2007).
17. J. Kašpar and P. Fornasiero, *J. Solid State Chem.*, **171**(1-2), 19 (2003).
18. M. Karppinen, H. Yanauchi and S. Otani, *Chem. Mater.*, **18**(2), 490 (2006).
19. S. Kadota, M. Kappinen, T. Motohashi and H. Yamauchi, *Chem. Mater.*, **20**(20), 6378 (2008).
20. S. Wang, H. S. Hao, B. F. Zhu, J. F. Jia and X. Hu, *J. Mater. Sci.*, **43**(15), 5385 (2008).
21. S. M. Zhang, MA Dissertation, ZhengZhou University (2011).
22. L. J. Guo, MA Dissertation, ZhengZhou University (2005).
23. L. P. Kozeeva, M. Y. Kameneva, A. N. Lavrov and N. V. Podberezskaya, *Inorg. Mater.*, **49**(6), 626 (2013).
24. O. Parkkima, H. Yamauchi and M. Karppinen, *Chem. Mater.*, **25**(4), 599 (2013).
25. M. Valldor, *Solid State Sci.*, **7**(10), 1163 (2005).
26. L. M. Hou, Q. B. Yu, K. Wang, T. Wang, F. Yang and S. Zhang, *J. Therm. Anal. Calorim.*, **49**(1), 317 (2019).
27. L. M. Hou, Q. B. Yu, K. Wang, S. Zhang, Q. Qin and F. Yang, *Korean J. Chem. Eng.*, **36**(1), 84 (2019).
28. A. D. Qi, S. D. Wang, G. Z. Fu, C. J. Ni and D. Y. Wu, *Appl. Catal. A: Gen.*, **281**(1-2), 233 (2005).
29. B. B. Shi and Z. D. Jiang, *Nat. Gas Chem. Ind.*, **38**(3), 11 (2013).
30. Wang, K. MA Diss., Shanghai Jiaotong University (2009).
31. S. Cimino, L. Lisi, R. Pirone, G. Russo and M. Turco, *Catal. Today*, **59**(1), 19 (2000).
32. K. Wang, Q. B. Yu, Q. Qin, Z. L. Zuo and T. W. Wu, *Chem. Eng. J.*, **287**, 292 (2016).
33. Q. Liu, J. J. Shi, S. D. Zheng, M. N. Tao, Y. He and Y. Shi, *Ind. Eng. Chem. Res.*, **53**(29), 11677 (2014).
34. L. M. Hou, Q. B. Yu, T. Wang, K. Wang, Q. Qin and Z. F. Qi, *Korean J. Chem. Eng.*, **35**(3), 626 (2018).
35. A. A. Yaremchenko, M. V. Patrakeev, V. V. Kharton, F. M. B. Marques, I. A. Leonidov and V. L. Kozhevnikov, *Solid State Sci.*, **6**(4), 357 (2004).